

1 **Frequency, magnitude and character of hyperthermal**  
2 **events at the onset of the Early Eocene Climatic**  
3 **Optimum**

4 **V. Lauretano<sup>1</sup>, K. Littler<sup>2,\*</sup>, M. Polling<sup>1</sup>, J. C. Zachos<sup>2</sup>, L. J. Lourens<sup>1</sup>**

5 [1]{Department of Earth Sciences, Faculty of Geosciences, Utrecht University,  
6 Budapestlaan 4, 3584CD, Utrecht, The Netherlands}

7 [2]{ Department of Earth and Planetary Sciences, University of California Santa Cruz,  
8 1156 High Street, Santa Cruz, CA 95064, USA}

9 [\*]{now at: Camborne School of Mines, University of Exeter, Penryn Campus,  
10 Penryn, Cornwall, TR10 9FE, United Kingdom}

11 Correspondence to: Vittoria Lauretano ([v.lauretano@uu.nl](mailto:v.lauretano@uu.nl))

12

13 **Abstract**

14 Recent studies have shown that the Early Eocene Climatic Optimum (EECO) was  
15 preceded by a series of short-lived global warming events, known as hyperthermals.  
16 Here we present high-resolution benthic stable carbon and oxygen isotope records  
17 from ODP Sites 1262 and 1263 (Walvis Ridge, SE Atlantic) between ~54 and ~52  
18 million years ago, tightly constraining the character, timing, and magnitude of six  
19 prominent hyperthermal events. These events, that include Eocene Thermal  
20 Maximum (ETM) 2 and 3, are studied in relation to orbital forcing and long-term  
21 trends. Our findings reveal an almost linear relationship between  $\delta^{13}\text{C}$  and  $\delta^{18}\text{O}$  for all  
22 these hyperthermals, indicating that the eccentricity-paced co-variance between deep-  
23 sea temperature changes and extreme perturbations in the exogenic carbon pool  
24 persisted during these events towards the onset of the EECO, in accord with previous  
25 observations for the Paleocene Eocene Thermal Maximum (PETM) and ETM2. The  
26 covariance of  $\delta^{13}\text{C}$  and  $\delta^{18}\text{O}$  during H2 and I2, which are the second pulses of the  
27 “paired” hyperthermal events ETM2-H2 and I1-I2, deviates with respect to the other  
28 events. We hypothesize that this could relate to a relatively higher contribution of an

29 isotopically heavier source of carbon, such as peat or permafrost, and/or to climate  
30 feedbacks/local changes in circulation. Finally, the  $\delta^{18}\text{O}$  records of the two sites show  
31 a systematic offset with on average 0.2‰ heavier values for the shallower Site 1263,  
32 which we link to a slightly heavier isotope composition of the intermediate water  
33 mass reaching the northeastern flank of the Walvis Ridge compared to that of the  
34 deeper northwestern water mass at Site 1262.

35

## 36 **1 Introduction**

37 The early Paleogene was characterized by a highly dynamic climatic system both on  
38 long- ( $>10^6$  years) and short- ( $< 10^4$  years) time scales. From the late Paleocene ( $\sim 58$   
39 Ma) to the early Eocene ( $\sim 50$  Ma), Earth's surface experienced a long-term warming  
40 trend that culminated in an extended period of extreme warmth, called the Early  
41 Eocene Climatic Optimum (EECO, Ma; Zachos et al., 2001, 2008; Bijl et al., 2009;  
42 Westerhold and Röhl, 2009). During the EECO, global temperatures reached a long-  
43 term maximum lasting about 2 Myrs, characterized by the warmest temperatures of  
44 the Cenozoic (Zachos et al., 2008). Superimposed on the long-term warming trend  
45 were a series of short-lived global warming (hyperthermal) events, accompanied by  
46 the release of  $^{13}\text{C}$ -depleted carbon into the ocean-atmosphere carbon reservoirs  
47 (Zachos, 2005; Lourens et al., 2005; Nicolo et al., 2007; Littler et al., 2014; Kirtland  
48 Turner et al., 2014). These events are of particular interest as they represent useful  
49 analogs for the current global warming, despite differences in background climatic  
50 conditions and rates of change (e.g., Zachos et al., 2008; Hönisch et al., 2012; Zeebe  
51 and Zachos, 2013).

52 The Paleocene Eocene Thermal Maximum (PETM or ETM1,  $\sim 56$  Ma), lasting less  
53 than 200 kyr, was the most extreme of these episodes. During the PETM global  
54 temperature rose by  $5\text{--}8^\circ\text{C}$ , and massive amounts of carbon were released as  
55 evidenced by a significant negative carbon isotope excursion (CIE) of  $>3\text{‰}$  in the  
56 ocean/atmosphere carbon pools, and widespread dissolution of seafloor carbonate  
57 (Kennett and Stott, 1991; Dickens et al., 1995; Thomas and Shackleton, 1996;  
58 Zachos, 2005; Sluijs et al., 2007; Zachos et al., 2008; McInerney and Wing, 2011). A  
59 series of similar events are recorded in carbonate records from marine and continental  
60 deposits from the early Paleogene, as expressed by negative excursions in  $\delta^{13}\text{C}$  and  
61  $\delta^{18}\text{O}$  often accompanied by dissolution horizons (e.g., Cramer et al., 2003; Lourens et

62 al., 2005; Agnini et al., 2009; Galeotti et al., 2010; Stap et al., 2010; Zachos et al.,  
63 2010; Abels et al., 2012; Slotnick et al., 2012; Kirtland Turner et al., 2014; Littler et  
64 al., 2014; Abels et al., 2015). Orbitally tuned records for this geological interval  
65 provide evidence that the early Eocene hyperthermal events were paced by variations  
66 in the Earth's orbit, specifically in the long and short eccentricity cycles. (e.g., Cramer  
67 et al., 2003; Lourens et al., 2005; Littler et al., 2014; Zachos et al., 2010; Sexton et al.,  
68 2011).

69 Several different carbon sources have been proposed to explain the negative CIE,  
70 including: (1) the release of methane by thermal dissociation of gas hydrates on the  
71 continental slopes (Dickens et al., 1995); (2) the burning of peat and coal deposits  
72 (Kurtz et al., 2003); and (3) the release of carbon from thawing of permafrost soils at  
73 high latitudes as a feedback or as a direct response to orbital forcing (Deconto et al.,  
74 2012); while (4) a redistribution of  $^{13}\text{C}$ -depleted carbon within oceans has been  
75 proposed as mechanism for hyperthermals in the early to middle Eocene interval  
76 (Sexton et al., 2011).

77 Despite the uncertainty in carbon source and triggering mechanism of the  
78 hyperthermal events, a common reservoir has been theorized to explain the consistent  
79 covariance in benthic foraminiferal  $\delta^{13}\text{C}$  and  $\delta^{18}\text{O}$  across both the PETM and ETM2,  
80 indicating that changes in the exogenic carbon pool were similarly related to warming  
81 during these events (Stap et al., 2010). The aim of this paper is to test this relationship  
82 by constraining the relative timing and magnitude of changes in deep ocean  
83 temperatures and carbon isotope excursions for a series of carbon isotope excursions  
84 that succeed ETM2, initially identified by Cramer et al., (2003) in the composite bulk  
85 carbonate  $\delta^{13}\text{C}$  record from several deep-sea sites (ODP Sites 690 and 1051; DSDP  
86 Site 550 and 577). For this purpose, we generated high-resolution carbon and oxygen  
87 stable isotope records of the benthic foraminiferal species *Nuttalides truempyi* from  
88 ODP Sites 1262 and 1263 (Walvis Ridge) encompassing the interval from the ETM2  
89 (Stap et al., 2010) to the ETM3 (Röhl et al. 2005), providing the first complete high-  
90 resolution benthic stable isotope records for the early Eocene events leading to the  
91 onset of the EECO.

92

93 **2 Materials and Methods**

94 **2.1 Site location and sampling**

95 ODP Sites 1262 and 1263 represent the deepest and shallowest end-member of a 2-  
96 km depth transect recovered during ODP Leg 208. Site 1263 is located just below the  
97 crest of the northeast flank of Walvis Ridge, in the southeastern Atlantic, at a water  
98 depth of 2717 m, whereas Site 1262 was drilled near the base of the northwestern  
99 flank of Walvis Ridge at a water depth of 4759 m (Fig. 1). The estimated paleodepths  
100 of Sites 1262 and 1263 at ~56 Ma were ~3600 m and 1500 m, respectively (Zachos et  
101 al., 2004). The material recovered at the two sites provided an expanded sequence of  
102 early Paleogene sediments, yielding a complete section mainly composed of  
103 calcareous nannofossil ooze, chalk and marls. The composite depth scale for Site  
104 1263 was constructed using the magnetic susceptibility (MS) and sediment lightness  
105 ( $L^*$ ) from the four holes (Zachos et al., 2004).

106 Samples were collected at the Bremen Core Repository from Holes A, B and C for  
107 Site 1263, and Holes A and B for Site 1262, according to the shipboard meters  
108 composite depth section (mcd) (Zachos et al., 2004). A 28-m thick interval of Site  
109 1263 was sampled at a resolution of 5 cm from ~268 to ~296 mcd, and a ~6-m  
110 interval of Site 1262 was sampled at a resolution of 3 cm from ~103 to ~109 mcd  
111 (Fig. 3). Prior to the analyses, samples were freeze dried, washed and sieved to obtain  
112 fractions larger than 38, 63 and 150  $\mu\text{m}$  at University of California, Santa Cruz and  
113 Utrecht University.

114

115 **2.2 Stable isotopes**

116 Multi-specimen samples of *N. truempyi* were picked from the >150  $\mu\text{m}$  fraction. The  
117 stable isotope values of picked specimens (average of 6–8 foraminiferal calcite tests)  
118 from Site 1263 were carried out at Utrecht University using a CARBO-KIEL  
119 automated carbonate preparation device linked on-line to a Thermo-Finnigan  
120 MAT253 mass spectrometer. Calibrations to the international standard (NBS-19) and  
121 to the in-house standard (Naxos marble) show an analytical precision of 0.03‰ and  
122 0.08‰ for  $\delta^{13}\text{C}$  and  $\delta^{18}\text{O}$ , respectively. The stable isotope values of picked specimens

123 from Site 1262 were analyzed on a KIEL IV carbonate preparation device linked on-  
124 line to a Thermo-Finnigan MAT253 mass spectrometer, at the UCSC Stable Isotope  
125 Laboratory, Santa Cruz. Calibrations to the in-house standard Carrara marble (CM05)  
126 and international standards (NBS-18 and NBS-19) yield an analytical precision of  
127 0.05‰ and 0.08‰, for  $\delta^{13}\text{C}$  and  $\delta^{18}\text{O}$ , respectively. All values are reported in  
128 standard delta notation relative to VPDB (Vienna Pee Dee Belemnite). Outliers were  
129 defined by adding or subtracting an upper and lower boundary of  $2\sigma$  from a 13-points  
130 moving average, following the method by Liebrand et al. (2011). Published benthic  
131 isotope data of the same foraminiferal species for the ETM2 (or H1/Elmo event) and  
132 H2 were included in this study to obtain a longer continuous record of Site 1263 and  
133 1262 (Stap et al., 2010) and for I1-I2 of Site 1262 (Littler et al., 2014)  
134

### 135 **2.3 Paleotemperature reconstructions**

136 Paleotemperatures were obtained from the benthic foraminiferal  $\delta^{18}\text{O}$  values by  
137 applying the equation of Bemis et al. (1998):

$$138 \quad T(^{\circ}\text{C}) = 16.9 - 4.38 (\delta^{18}\text{O}_c - \delta^{18}\text{O}_{\text{sw}}) + 0.10 (\delta^{18}\text{O}_c - \delta^{18}\text{O}_{\text{sw}})^2 \quad (1)$$

139 The temperature scale is computed assuming an ice-free sea water ( $\delta^{18}\text{O}_{\text{sw}}$ ) value of -  
140 1.2‰ (VPDB). This value is calculated correcting the estimated deep sea  $\delta^{18}\text{O}_{\text{sw}}$  value  
141 of -0.98‰ (SMOW) relative to PDB scales by subtracting 0.27‰ (Hut, 1987). The *N.*  
142 *truempyi*  $\delta^{18}\text{O}$  was adjusted for disequilibrium vital effects by adding 0.35‰  
143 (Shackleton et al., 1984; Shackleton and Hall, 1997), assuming that the isotopic  
144 disequilibrium for this species remained constant through time.

145

### 146 **3 Age model**

147 Given the typical low resolution age control afforded by magneto- and bio-  
148 stratigraphy, and the availability of a robust cycle (i.e., orbital) based chronology for  
149 the Leg 208 sites (Westerhold et al., 2007), we developed an eccentricity-tuned age  
150 model for the studied interval using the red over green color ratio ( $a^*$ ) records of ODP  
151 Sites 1263 and 1262 (Fig. 2). For tuning, we applied first spectral analysis in the  
152 depth domain using standard Blackman-Tukey and Gaussian filtering techniques as  
153 provided by the AnalySeries program (Paillard et al., 1996). Site 1262, the deepest

154 site at Walvis Ridge, was chosen as the backbone for our tuning. The a\* record of this  
155 site clearly revealed a ~3-m period, interpreted as reflecting the climatic imprint of the  
156 405-kyr eccentricity cycle (Lourens et al., 2005). Subsequently, we filtered this  
157 component and tuned it directly to the extracted 405-kyr eccentricity component of  
158 the La2010d orbital solution (Laskar et al., 2011) with maximum a\* values,  
159 interpreted to represent maximum carbonate dissolution, corresponding to maximum  
160 eccentricity values (Table 1). A similar approach was carried out for the a\* record of  
161 Site 1263 to evaluate the continuity of the successions and robustness of the filtered  
162 output (Fig. 2). Finally, the tuned age model of Site 1262 was transferred to Site 1263  
163 by correlating >50 characteristic features in the a\* records of both sites as tie points  
164 (Fig.2 and Table 2).

165 Different tuning options have been debated in the last 10 years, resulting in an age for  
166 the PETM ranging between ~55.5 and ~56.3 My (Lourens et al., 2005; Westerhold et  
167 al., 2008; Hilgen et al., 2010, Dinarès-Turell et al., 2014). Here we report on two  
168 tuning options (Fig. 2), assigning an age of  $53.69 \pm 0.02$  (option 1) or of  $54.09 \pm 0.02$   
169 (option 2) to ETM2 (Westerhold et al., 2007). According to both options, ETM2  
170 predates the 405-kyr maximum falling at an increasing limb, in agreement with  
171 observations of Westerhold et al. (2007), but in contrast with the earlier interpretation  
172 by Lourens et al. (2005), who aligned this event to a maximum in the 405-kyr cycle.  
173 Recent literature revising the Paleocene cyclostratigraphic interpretation (Dinarès-  
174 Turell et al., 2014; Hilgen et al., 2015) have shown that the Paleocene holds 25, rather  
175 than 24, 405-kyr eccentricity cycles. In addition, new U/Pb ages have become  
176 available which support an age of ~66.0 Ma for the K/Pg boundary (Kuiper et al.,  
177 2008; Renne et al., 2013). These developments point to an age of ~54.0 Ma for ETM2  
178 and therefore we plot our results anchoring the age of ETM2 to option 2 (Fig. 4).  
179 Evolutionary wavelet spectra were obtained in the time domain using the wavelet  
180 script of Torrence and Compo (<http://paos.colorado.edu/research/wavelets>). Prior to  
181 the analysis, carbon and oxygen records were resampled at 2.5 kyrs, detrended and  
182 normalized.

183

#### 184 **4 Results**

185 Our new benthic  $\delta^{13}\text{C}$  and  $\delta^{18}\text{O}$  records show six major negative excursions between  
186 54 and 52 Ma (Fig. 4). They correspond to the ETM2, H2, I1, I2, J, and ETM3/X/K

187 events, formerly recognized in deep-sea  $\delta^{13}\text{C}$  bulk carbonate records and land-based  
188 marine and continental sections (Abels et al., 2012; Agnini et al., 2009; Cramer et al.,  
189 2003; Kirtland Turner et al., 2014; Littler et al., 2014; Lourens et al., 2005; Slotnick et  
190 al., 2012; Abels et al., 2015)

191 The general long-term trend in our ~2 Myr long records indicates a minor increase  
192 between 54.2 Ma and 53.2 Ma followed by an average decrease of ~0.3 ‰ in absolute  
193 values of both  $\delta^{13}\text{C}$  and  $\delta^{18}\text{O}$  baseline values following J (~53.1 Ma), with minor  
194 cycles evident between the six main events in both records. Following J, both records  
195 maintain rather stable values up to ETM3 (Fig. 4). These changes are negligible  
196 compared to the Paleocene-Eocene long-term warming trend and long-term negative  
197 trend in carbon isotope values. However, the onset of more generally negative  $\delta^{13}\text{C}$   
198 values, coinciding with J, has also been observed in the deep-sea bulk carbonate  
199 record at Site 1262 (Zachos et al., 2010) and in the land-based section at Mead Stream  
200 by Slotnick et al. (2012), who suggested that the pronounced change in lithology  
201 beginning with J could be used as a chronostratigraphic marker for the onset of the  
202 EECO.

203 Evidence for the onset of warmer temperatures leading to the EECO is evident at ~53  
204 Ma in the benthic  $\delta^{18}\text{O}$  records at both Sites 1262 and 1263 (Fig. 4). Baseline average  
205  $\delta^{18}\text{O}$  values prior to ETM2, signifying the response of the unperturbed oceanic  
206 system, represent a mean deep-sea temperature of ~12°C, which post-J increases by  
207 >0.5°C. Despite variability, our data shows that this increase in background  
208 temperature continued upwards across ETM3. Here we suggest that the onset of the  
209 EECO can be identified in our records with the onset of the general low in benthic  
210 isotope values initiated with J (~53 Ma) and thus including ETM3 within the EECO.  
211 Although longer high-resolution benthic  $\delta^{18}\text{O}$  records are needed to establish the total  
212 duration of the EECO, this could represent a first step towards a formal definition of  
213 the warmest interval of the Cenozoic, avoiding ambiguity caused by changes in the  
214 time scale.

215 On the short-term scale, our new data across the events following ETM2 and H2  
216 indicate a rise in temperature of ~2 °C and ~1.5 °C during I1 and I2, respectively. The  
217 J-event was associated with a temperature increase of >1°C superimposed on the  
218 further average decrease in baseline  $\delta^{18}\text{O}$  value. The ETM3 is expressed in both the

219 shallowest and deepest site at Walvis Ridge by similar isotopic excursions, with a CIE  
220 of  $\sim 0.8\%$  and a negative shift in the  $\delta^{18}\text{O}$  record of  $\sim 0.5\%$ , corresponding to a  
221 warming in the deep ocean of  $2\text{--}2.5^\circ\text{C}$ , comparable to values observed during the  
222 ETM2 (Stap et al., 2010).

223 Evolutionary wavelet analyses for  $\delta^{13}\text{C}$  and  $\delta^{18}\text{O}$  records of Site 1263 show spectral  
224 power concentrated at distinct frequencies, corresponding to the long 405-kyr and  
225 short  $\sim 100$ -kyr eccentricity cycles (Fig. 5). The isotope records reveal coherent  
226 patterns, with the highest spectral power concentrated during the ETM2–H2 and I1–  
227 I2. The  $\sim 100$ -kyr signal in  $\delta^{13}\text{C}$ , which is very prominent in the first 1 Myr of the  
228 record, weakens after J. The imprint of precession and/or obliquity forcing is very  
229 weak/absent throughout the entire record. As a result of our tuning approach, minima  
230 in  $\delta^{13}\text{C}$  are approximately in phase with maxima in the 405-kyr and  $\sim 100$ -kyr  
231 eccentricity cycles, following previous work (e.g., Cramer et al. 2003; Lourens et al.,  
232 2005; Zachos et al., 2010; Stap et al., 2010).

## 233 **5 Discussion**

### 234 **5.1 Isotope covariance**

235 Our high-resolution benthic isotope records provide a direct constraint on the  
236 relationship between the temperature-related signal carried by the benthic  
237 foraminiferal  $\delta^{18}\text{O}$  and the CIEs during the events leading to the EECO. The six  
238 events recognised in the benthic records vary in terms of both the magnitude of the  
239 CIEs and the inferred temperature changes. The most intense perturbations are  
240 associated with the ETM2, I1 and ETM3, whereas H2 and I2, which lag the larger  
241 events by one 100-kyr eccentricity cycle, are less prominent (Fig. 4). One important  
242 question then is whether all these events of varying magnitude are accompanied by  
243 the same source of light carbon released into the ocean atmosphere system and  
244 climatic response. Following Stap et al. (2010), we have assessed this by comparing  
245 the slopes of the regression line between the carbon and oxygen isotopes of the  
246 individual events (Fig. 6). These cross-plots clearly show that all events exhibit  
247 significant and coherent linear correlation in both sites with slopes ranging between  
248 0.5 and 0.7 (Figg. 6-7), indicating a consistent relationship for all events between  
249 changes in deep-sea temperatures and carbon release. We conclude that this  
250 significant covariance between the benthic  $\delta^{13}\text{C}$  and  $\delta^{18}\text{O}$  records suggests a strong



251 non-linear response to orbital forcing of global temperatures and the release of  
252 isotopically light carbon (e.g. methane gas and/or CO<sub>2</sub>) into the ocean-atmosphere  
253 system during eccentricity maxima, driving subsequent carbonate dissolution and  
254 enhanced greenhouse warming, as has been observed in the older part of the record at  
255 Site 1262 (Stap et al., 2010; Littler et al., 2014). This conclusion is further underlined  
256 by the consistent scaling of CIE magnitudes between our deep-sea data and soil  
257 nodule records of the Bighorn basin for these events, which strengthens the  
258 hypothesis of a similar isotopic composition of the carbon source for the early Eocene  
259 hyperthermal events (Abels et al., 2015).

260

## 261 **5.2 The “paired” hyperthermal events**

262 The slopes of the regression lines for H2 and I2 appear slightly steeper than those of  
263 ETM2, I1, J and ETM3 (Fig. 6). To statistically test this (dis)similarity, we applied a  
264 student t-test to pairs of slopes, comparing all the events against each other using both  
265 a pooled and an unpooled error variance. The results show that the null hypothesis  
266 (the slopes being similar,  $\alpha=0.05$ ) is satisfied in the case of ETM2, I1, J and ETM3.  
267 The tests on the steeper slopes of H2 and I2 generally display values of  $p \leq 0.05$  when  
268 tested against the other events, but values of  $p \geq 0.05$  when tested against each other.  
269 This implies that the smaller events, H2 and I2, are statistically similar to each other  
270 but differ slightly from the other perturbations. Even though this statistical approach  
271 might be subject to limitations derived from the range of data points chosen for each  
272 event, it clearly shows that the slopes for H2 and I2 deviate from the average values  
273 given by the other events. Moreover, the statistical deviation of the slopes of H2 and  
274 I2 is clearer when comparing them with the average slope for all events of the two  
275 sites, since they fall outside the (99.99%) confidence limits (Fig. 7). The average  
276 slope between  $\delta^{13}\text{C}$  and  $\delta^{18}\text{O}$  of 0.6 for both sites is also in accord with previous  
277 observations for the onset/recovery of PETM, ETM2 and H2 by Stap et al., (2010).

278 The “paired” hyperthermal events, ETM2–H2 and I1–I2 thus reveal slightly different  
279  $\delta^{13}\text{C}$  vs.  $\delta^{18}\text{O}$  relationships between their first (ETM2 and I1) and secondary (H2 and  
280 I2) pulses. Assuming that these signals are globally representative, this could imply  
281 that the second of the two pulses had a relatively larger contribution of an isotopically  
282 heavier carbon source than the first pulse. Such a mechanism could hint to a methane-  
283 related dominant carbon source (e.g. methane hydrates) during the initial phase of the

284 paired hyperthermal events that is mostly depleted, so that other relatively heavier  
285 carbon isotope sources (e.g. wetlands, peat) become progressively more important  
286 during the successive event. Warming of intermediate water during ETM2 and I1, as  
287 was previously been suggested for the PETM and ETM2 (Jennions et al., 2015; Lunt  
288 et al., 2010), could have destabilized methane clathrates leading to their dissociation  
289 and the subsequent increased warming and large CIE. Mechanisms related to the  
290 depletion and subsequent recharge time of the inferred methane clathrate reservoir  
291 between ETM2 and H2, and I1 and I2, could explain why the second event had both a  
292 smaller magnitude and possibly a smaller relative contribution of methanogenic  
293 carbon. The smaller magnitude of the two secondary carbon pulses, regardless of the  
294 isotopic composition of their source, seems feasible because the  $a^*$  values, interpreted  
295 as representative of the degree of carbonate dissolution, were significantly lower than  
296 during their preceding counterparts (Fig. 2). In other words, the degree of carbonate  
297 dissolution associated with the shoaling of the calcite compensation depth (CCD) and  
298 lysocline appears to be less severe than during the first pulses. In this respect it is  
299 worth noting that H2 and I2 also behave differently from the “larger” events in terms  
300 of biotic disruption. During the PETM, ETM2 and I1, rates of variability in  
301 planktonic communities indicate that the biotic response was proportionate to the  
302 magnitude of carbon injections, and biotic disruption linearly declined with the  
303 decreasing size of CIEs (Gibbs et al., 2012; Jennions et al., 2015). However, H2 and  
304 I2 do not show evidence of above-background variance, suggesting that during these  
305 events the system apparently failed to cross the environmental “threshold” necessary  
306 to generate a detectable marine biotic disruption (D’haenens et al., 2012; Gibbs et al.,  
307 2012). This all suggests that a change in the climate feedbacks and/or an incomplete  
308 recovery of the buffering capacity of the ocean system after the first perturbation  
309 could have played a significant role in amplifying the temperature response during the  
310 secondary pulse. On the other hand, we cannot dismiss the possibility that local  
311 circulation changes and/or partial dissolution slightly altered the anomalies in  $\delta^{18}\text{O}$   
312 and  $\delta^{13}\text{C}$  during H2 and I2 at Walvis Ridge. Further research is hence needed to ratify  
313 the (global) significance of this finding.

314

### 315 **5.3 Thresholds and orbital pacing**

316 The transition towards the EECO is marked by a general decrease of both benthic  
317 carbon and oxygen isotopic values of  $\sim 0.3\text{‰}$  at Site 1263, indicative of both long-  
318 term warming and progressive oxidation of organic matter releasing  $\text{CO}_2$  into the  
319 ocean-atmosphere system. It has been theorized that the timing and magnitude of the  
320 hyperthermals would respond to the crossing of a thermal threshold, more frequently  
321 reached in phases of orbital-driven temperature increase (Lourens et al., 2005; Lunt et  
322 al., 2011). In addition, the carbon reservoir or capacitor (Dickens, 2003), regardless of  
323 its nature and as a result of the long-term temperature increase between the late  
324 Paleocene–early Eocene, would be largely depleted by the peak of the EECO, leading  
325 to an interval free of hyperthermals. In turn, a series of orbitally paced global  
326 warming events of decreasing frequency and increased size are expected to occur  
327 during the post-EECO cooling phase when the carbon reservoir would have been  
328 progressive refilled (e.g., Kirtland Turner et al., 2014). This hypothesis has been  
329 questioned with data from a composite bulk stable isotope record of Site 1258  
330 showing that a series of negative isotope excursions continued throughout the EECO.  
331 This evidence suggests that episodes of carbon release persisted during the peak of  
332 warmth and the onset of the cooling trend (Kirtland Turner et al., 2014). Kirtland  
333 Turner and co-authors (2014) suggest that the mechanisms operating in the early  
334 Eocene climate were not necessarily exceptional but actually similar to those invoked  
335 for the Oligocene and Miocene when cyclic variations in the carbon cycle were also  
336 clearly paced by orbital forcing, particularly in the eccentricity bands (Holbourn et al.,  
337 2007; Pälike et al., 2006; Zachos et al., 2001b). Although the carbon and oxygen  
338 isotope records of the Oligocene-Miocene and early Eocene are certainly paced by  
339 eccentricity, their appearance in terms of punctuation are clearly different. In  
340 particular, a relatively sudden release (storage) of large amounts of light carbon (e.g.  
341 methane hydrates) into the ocean atmosphere system seems the only way to explain  
342 the unusual magnitude of the CIEs recorded at Walvis Ridge given the rate/magnitude  
343 of warming, as well as the carbonate dissolution and changes in benthic assemblages  
344 associated with those events (Jennions et al., 2015; Stap et al., 2009).

345

#### 346 **5.4 Site 1263 vs. Site 1262**

347 Comparison between the benthic  $\delta^{13}\text{C}$  and  $\delta^{18}\text{O}$  records of Sites 1263 and 1262  
348 reveals an almost identical pattern, although  $\delta^{18}\text{O}$  values of Site 1263 are consistently  
349  $\sim 0.2\text{‰}$  heavier than those of Site 1262 (Fig. 3 and 4). A similar (reversed) pattern has  
350 been previously observed by Stap et al. (2009) in the case of ETM2, and attributed to  
351 differential dissolution from the shallowest to the deepest site. Conversely, selective  
352 dissolution seems unlikely to justify the persistent offset in  $\delta^{18}\text{O}$  values observed  
353 throughout the new post-ETM2 record presented herein. We posit that this offset may  
354 be linked to a different average isotopic composition of the water masses at those  
355 sites. Accordingly, the intermediate water mass reaching Site 1263 were more  $^{18}\text{O}$ -  
356 enriched than the deeper waters at Site 1262. The existence of a discrete intermediate  
357 water body in the early Eocene South Atlantic is supported by recent benthic  
358 foraminiferal assemblage, sedimentological evidence and Earth system modeling data  
359 across ETM2, which suggests that warming in the intermediate waters bathing Site  
360 1263 led to differential patterns in sedimentary and ecological data between this site  
361 and the deeper Site 1262 (Jennions et al., 2015).

#### 362 **6 Conclusions**

363 New high-resolution benthic stable isotope records from ODP Sites 1262 and 1263  
364 provide a detailed framework to explore the (transient) nature of early Eocene  
365 hyperthermal events during the onset of the EECO. Our results further confirm the  
366 link between large-scale carbon release and climate response to orbital forcing, in  
367 particular to short- and long- eccentricity cycles. The transition towards the EECO is  
368 marked by a general decrease of both benthic carbon and oxygen isotopic values of  
369  $\sim 0.3\text{‰}$  at Site 1263, indicative of both long-term warming and progressive oxidation  
370 of organic matter releasing  $\text{CO}_2$  into the ocean-atmosphere system. Consistent  
371 covariance between benthic carbon and oxygen isotopes demonstrates that global  
372 temperatures and changes in the exogenic carbon pool were similarly coupled during  
373 each of the studied hyperthermal events. In this regard, we found that the second  
374 pulses of the paired hyperthermal events (i.e. H2 and I2) point to a slightly different  
375 behaviour. Whether this implies a larger role for a carbon reservoir characterized by a  
376 heavier isotopic signature remains debatable and, hence, allows for further  
377 consideration of other operational processes such as local circulation changes, partial  
378 dissolution, or different climate feedbacks. Finally we found a constant offset in

379 oxygen isotopic values between Site 1263 and 1262, with the isotopic composition of  
380 the shallower waters at Site 1263 consistently heavier than at Site 1262, suggesting  
381 presence of a discrete water body at intermediate depths of the Walvis Ridge transect.

## 382 **Acknowledgements**

383 We are grateful to Gerard Dickens, Lee Kump and Philip Sexton for their constructive  
384 comments. We thank the International Ocean Discovery Program (IODP) for  
385 providing the samples used in this study. We also thank A. van Dijk at Utrecht  
386 University, and Dyke Andreassen and Chih-Ting Hsieh at UCSC for analytical  
387 support. This research was funded by NWO-ALW grant (project number 865.10.001)  
388 to L.J. Lourens. We thank F. Hilgen and H.A. Abels for providing valuable comments  
389 on the manuscript.

390 **References**

- 391 Abels, H. A., Clyde, W. C., Gingerich, P. D., Hilgen, F. J., Fricke, H. C., Bowen, G.  
392 J. and Lourens, L. J.: Terrestrial carbon isotope excursions and biotic change during  
393 Palaeogene hyperthermals, *Nat. Geosci.*, 5(5), 326–329, doi:10.1038/ngeo1427, 2012.
- 394 Abels, H. A., Lauretano, V., van Yperen, A., Hopman, T., Zachos, J. C., Lourens, L.  
395 J., Gingerich, P. D., Bowen, G.J.: Carbon isotope excursions in paleosol carbonate  
396 marking five early Eocene hyperthermals in the Bighorn Basin, Wyoming, *Clim. Past*  
397 Discussion, <http://www.clim-past-discuss.net/11/1857/2015/cpd-11-1857-2015.html>.
- 398 Agnini, C., Macri, P., Backman, J., Brinkhuis, H., Fornaciari, E., Giusberti, L.,  
399 Luciani, V., Rio, D., Sluijs, A. and Speranza, F.: An early Eocene carbon cycle  
400 perturbation at ~52.5 Ma in the Southern Alps: Chronology and biotic response,  
401 *Paleoceanography*, 24(2), doi:10.1029/2008PA001649, 2009.
- 402 Bemis, B.E., Spero, H.J., Bijma, J., and Lea, D.W.: Reevaluation of the oxygen  
403 isotopic composition of planktonic foraminifera: Experimental results and revised  
404 paleotemperature equations: *Paleoceanography*, v. 13, p. 150-160, 1998.
- 405 Bijl, P. K., Schouten, S., Sluijs, A., Reichart, G.-J., Zachos, J. C. and Brinkhuis, H.:  
406 Early Palaeogene temperature evolution of the southwest Pacific Ocean., *Nature*,  
407 461(7265), 776–9, doi:10.1038/nature08399, 2009.
- 408 Cramer, B. S., Wright, J. D., Kent, D. V and Aubry, M.-P.: Orbital climate forcing of  
409  $\delta^{13}\text{C}$  excursions in the late Paleocene–early Eocene (chrons C24n–C25n),  
410 *Paleoceanography*, 18(4), doi:10.1029/2003PA000909, 2003.
- 411 D’haenens, S., Bornemann, A., Stassen, P. and Speijer, R. P.: Multiple early Eocene  
412 benthic foraminiferal assemblage and  $\delta^{13}\text{C}$  fluctuations at DSDP Site 401 (Bay of  
413 Biscay — NE Atlantic), *Mar. Micropaleontol.*, 88-89, 15–35,  
414 doi:10.1016/j.marmicro.2012.02.006, 2012.
- 415 DeConto, R. M., Galeotti, S., Pagani, M., Tracy, D., Schaefer, K., Zhang, T., Pollard,  
416 D. and Beerling, D. J.: Past extreme warming events linked to massive carbon release  
417 from thawing permafrost., *Nature*, 484(7392), 87–91, doi:10.1038/nature10929, 2012.
- 418 Dickens, G. R.: Rethinking the global carbon cycle with a large, dynamic and  
419 microbially mediated gas hydrate capacitor, *Earth Planet. Sci. Lett.*, 213(3-4), 169–  
420 183, doi:10.1016/S0012-821X(03)00325-X, 2003.
- 421 Dickens, G.R, J.R. O’Neil, D.K. Rea, and R.M. Owen: Dissociation of oceanic  
422 methane hydrate as a cause of the carbon isotope excursion at the end of the  
423 Paleocene. *Paleoceanography* 10, 965-971, 1995.
- 424 Dinarès-Turell, J., Westerhold, T., Pujalte, V., Röhl, U. and Kroon, D.: Astronomical  
425 calibration of the Danian stage (Early Paleocene) revisited: Settling chronologies of  
426 sedimentary records across the Atlantic and Pacific Oceans, *Earth Planet. Sci. Lett.*,  
427 405, 119–131, doi:10.1016/j.epsl.2014.08.027, 2014.

- 428 Galeotti, S., Krishnan, S., Pagani, M., Lanci, L., Gaudio, A., Zachos, J. C., Monechi,  
429 S., Morelli, G. and Lourens, L. J.: Orbital chronology of Early Eocene hyperthermals  
430 from the Contessa Road section, central Italy, *Earth Planet. Sci. Lett.*, 290(1-2), 192–  
431 200, doi:10.1016/j.epsl.2009.12.021, 2010.
- 432 Gibbs, S. J., Bown, P. R., Murphy, B. H., Sluijs, A., Edgar, K. M., Pälike, H., Bolton,  
433 C. T. and Zachos, J. C.: Scaled biotic disruption during early Eocene global warming  
434 events, *Biogeosciences*, 9(11), 4679–4688, doi:10.5194/bg-9-4679-2012, 2012.
- 435 Hilgen, F. J., Abels, H. A., Kuiper, K. F., Lourens, L. J. and Wolthers, M.: Towards a  
436 stable astronomical time scale for the Paleocene: Aligning Shatsky Rise with the  
437 Zumaia – Walvis Ridge ODP Site 1262 composite, *Newsletters Stratigr.*, 48(1), 91–  
438 110, doi:10.1127/nos/2014/0054, 2015.
- 439 Hilgen, F. J., Kuiper, K. F. and Lourens, L. J.: Evaluation of the astronomical time  
440 scale for the Paleocene and earliest Eocene, *Earth Planet. Sci. Lett.*, 300(1-2), 139–  
441 151, doi:10.1016/j.epsl.2010.09.044, 2010.
- 442 Holbourn, A., Kuhnt, W., Schulz, M., Flores, J-A. and Andersen, N.: Orbitally-paced  
443 climate evolution during the middle Miocene “Monterey” carbon isotope excursion,  
444 *Earth Planet. Sci. Lett.* 261, 534–550, 2007.
- 445 Hönisch, B., Ridgwell, A., Schmidt, D. N., Thomas, E., Gibbs, S. J., Sluijs, A., Zeebe,  
446 R., Kump, L., Martindale, R. C., Greene, S. E., Kiessling, W., Ries, J., Zachos, J. C.,  
447 Royer, D. L., Barker, S., Marchitto, T. M., Moyer, R., Pelejero, C., Ziveri, P., Foster,  
448 G. L. and Williams, B.: The geological record of ocean acidification, *Science*,  
449 335(6072), 1058–63, doi:10.1126/science.1208277, 2012.
- 450 Hut, G.: Consultants group meeting on stable isotope reference samples for  
451 geochemical and hydrological investigations: Vienna, Austria, Report to Director  
452 General of the Institute of Atomic Energy Agency, 42, 1987.
- 453 Jennions, S. M., Thomas, E., Schmidt, D. N., Lunt, D., and Ridgwell, A.: Changes in  
454 benthic ecosystems and ocean circulation in the Southeast Atlantic across Eocene  
455 Thermal Maximum 2, *Paleoceanography*, 30, doi:10.1002/2015PA002821, 2015.
- 456 Kennett, J. P. and Stott, L. D.: Abrupt deep-sea warming, palaeoceanographic  
457 changes and benthic extinctions at the end of the Palaeocene, *Nature*, 353(6341), 225–  
458 229, doi:10.1038/353225a0, 1991.
- 459 Kirtland Turner, S., Sexton, P. F., Charles, C. D. and Norris, R. D.: Persistence of  
460 carbon release events through the peak of early Eocene global warmth, *Nat. Geosci.*,  
461 12(9), 1–17, doi:10.1038/ngeo2240, 2014.
- 462 Kuiper, K. F., Deino, a, Hilgen, F. J., Krijgsman, W., Renne, P. R. and Wijbrans, J.  
463 R.: Synchronizing rock clocks of Earth history., *Science*, 320(5875), 500–4,  
464 doi:10.1126/science.1154339, 2008.

- 465 Kurtz, A. C., Kump, L. R., Arthur, M. A., Zachos, J. C. and Paytan, A.: Early  
466 Cenozoic decoupling of the global carbon and sulfur cycles, *Paleoceanography*, 18(4),  
467 doi:10.1029/2003PA000908, 2003.
- 468 Laskar, J., Fienga, A., Gastineau, M., and Manche, H.: La2010: A new orbital  
469 solution for the long term motion of the Earth: *Astron. Astrophys.*, Volume 532, A89,  
470 2011.
- 471 Liebrand, D., Lourens, L. J., Hodell, D. a., De Boer, B., Van De Wal, R. S. W. and  
472 Pälike, H.: Antarctic ice sheet and oceanographic response to eccentricity forcing  
473 during the early Miocene, *Clim. Past*, 7(3), 869–880, doi:10.5194/cp-7-869-2011,  
474 2011.
- 475 Littler, K., Röhl, U., Westerhold, T. and Zachos, J. C.: A high-resolution benthic  
476 stable-isotope record for the South Atlantic: Implications for orbital-scale changes in  
477 Late Paleocene-Early Eocene climate and carbon cycling, *Earth Planet. Sci. Lett.*,  
478 401, 18–30, doi:10.1016/j.epsl.2014.05.054, 2014.
- 479 Lourens, L. J., Sluijs, A., Kroon, D., Zachos, J. C., Thomas, E., Röhl, U., Bowles, J.  
480 and Raffi, I.: Astronomical pacing of late Palaeocene to early Eocene global warming  
481 events., *Nature*, 435(7045), 1083–1087, doi:10.1038/nature03814, 2005.
- 482 Lunt, D. J., Valdes, P. J., Jones, T. D., Ridgwell, A., Haywood, A. M., Schmidt, D.  
483 N., Marsh, R. and Maslin, M.: CO<sub>2</sub>-driven ocean circulation changes as an amplifier  
484 of Paleocene-Eocene thermal maximum hydrate destabilization, *Geology*, 38(10),  
485 875–878, doi:10.1130/G31184.1, 2010.
- 486 Lunt, D. J., Ridgwell, A., Sluijs, A., Zachos, J. C., Hunter, S. and Haywood, A.: A  
487 model for orbital pacing of methane hydrate destabilization during the Palaeogene,  
488 *Nat. Geosci.*, 4(11), 775–778, doi:10.1038/ngeo1266, 2011.
- 489 McInerney, F. a. and Wing, S. L.: The Paleocene-Eocene Thermal Maximum: A  
490 Perturbation of Carbon Cycle, Climate, and Biosphere with Implications for the  
491 Future, *Annu. Rev. Earth Planet. Sci.*, 39(1), 489–516, doi:10.1146/annurev-earth-  
492 040610-133431, 2011.
- 493 Nicolo, M. J., Dickens, G. R., Hollis, C. J. and Zachos, J. C.: Multiple early Eocene  
494 hyperthermals: Their sedimentary expression on the New Zealand continental margin  
495 and in the deep sea, *Geology*, 35(8), 699, doi:10.1130/G23648A.1, 2007.
- 496 Paillard, D., Labeyrie, L., Yiou, P.: Macintosh program performs time-series analysis.  
497 *Eos Trans. AGU* 77, 379, 1996.
- 498 Pälike, H., Norris, R.D., Herrle, J.O., Wilson, P.A., Coxall, H.K., Lear, C.H.,  
499 Shackleton, N.J., Tripathi, A.K., Wade, B.S.: The heart- beat of the Oligocene climate  
500 system, *Science* 314, 1894–1998, 2006.
- 501 Renne, P. R., Deino, A. L., Hilgen, F. J., Kuiper, K. F., Mark, D. F., Mitchell, W. S.,  
502 Morgan, L. E., Mundil, R. and Smit, J.: Time scales of critical events around the



- 503 Cretaceous-Paleogene boundary., *Science*, 339(6120), 684–7,  
504 doi:10.1126/science.1230492, 2013.
- 505 Röhl, U., Westerhold, T., Monechi, S., Thomas, E., Zachos, J.C., Donner, B., 2005.  
506 The Third and Final Early Eocene Thermal Maximum: Characteristics, Timing and  
507 Mechanisms of the ‘X’ Event, GSA Annual Meeting 37. Geological Society of  
508 America, Salt Lake City, USA. 264 pp
- 509 Sexton, P. F., Norris, R. D., Wilson, P. a, Pälike, H., Westerhold, T., Röhl, U., Bolton,  
510 C. T. and Gibbs, S.: Eocene global warming events driven by ventilation of oceanic  
511 dissolved organic carbon, *Nature*, 471(7338), 349–352, doi:10.1038/nature09826,  
512 2011.
- 513 Shackleton, N. J., M. A. Hall, and A. Boersma: Oxygen and carbon isotope data from  
514 Leg-74 foraminifers, Initial Rep. Deep Sea Drill. Project, 74, 599–612, 1984.
- 515 Shackleton, N. J., and Hall, M. A: The late Miocene stable isotope record, Site 926,  
516 Proc. Ocean Drill. Program Sci. Results, 154, 367–373. doi:  
517 10.2973/odp.proc.sr.154.119.1997
- 518 Slotnick, B. S., Dickens, G. R., Nicolo, M. J., Hollis, C. J., Crampton, J. S., Zachos, J.  
519 C. and Sluijs, A.: Large-Amplitude Variations in Carbon Cycling and Terrestrial  
520 Weathering during the Latest Paleocene and Earliest Eocene: The Record at Mead  
521 Stream, New Zealand, *J. Geol.*, 120(5), 487–505, doi:10.1086/666743, 2012.
- 522 Sluijs, A., Brinkhuis, H., Schouten, S., Bohaty, S. M., John, C. M., Zachos, J. C.,  
523 Reichart, G.-J., Sinninghe Damsté, J. S., Crouch, E. M. and Dickens, G. R.:  
524 Environmental precursors to rapid light carbon injection at the Palaeocene/Eocene  
525 boundary., *Nature*, 450(7173), 1218–21, doi:10.1038/nature06400, 2007.
- 526 Stap, L., Lourens, L. J., Thomas, E., Sluijs, A., Bohaty, S. and Zachos, J. C.: High-  
527 resolution deep-sea carbon and oxygen isotope records of Eocene Thermal Maximum  
528 2 and H2, *Geology*, 38(7), 607–610, doi:10.1130/G30777.1, 2010.
- 529 Stap, L., Sluijs, A., Thomas, E. and Lourens, L. J.: Patterns and magnitude of deep  
530 sea carbonate dissolution during Eocene Thermal Maximum 2 and H2, Walvis Ridge,  
531 southeastern Atlantic Ocean, *Paleoceanography*, 24(1), doi:10.1029/2008PA001655,  
532 2009.
- 533 Thomas, E. and Shackleton, N. J.: The Paleocene-Eocene benthic foraminiferal  
534 extinction and stable isotope anomalies, *Geol. Soc. London, Spec. Publ.*, 101(1), 401–  
535 441, doi:10.1144/GSL.SP.1996.101.01.20, 1996.
- 536 Westerhold, T. and Röhl, U.: High resolution cyclostratigraphy of the early Eocene –  
537 new insights into the origin of the Cenozoic cooling trend, *Clim. Past Discuss.*, 5(1),  
538 495–534, 2009.
- 539 Westerhold, T., Röhl, U., Laskar, J., Raffi, I., Bowles, J., Lourens, L. J. and Zachos, J.  
540 C.: On the duration of magnetochrons C24r and C25n and the timing of early Eocene  
541 global warming events: Implications from the Ocean Drilling Program Leg 208

- 542 Walvis Ridge depth transect, *Paleoceanography*, 22(2), doi:10.1029/2006PA001322,  
543 2007.
- 544 Westerhold, T., Röhl, U., Raffi, I., Fornaciari, E., Monechi, S., Reale, V., Bowles, J.  
545 and Evans, H. F.: Astronomical calibration of the Paleocene time, *Palaeogeogr.*  
546 *Palaeoclimatol. Palaeoecol.*, 257(4), 377–403, doi:10.1016/j.palaeo.2007.09.016,  
547 2008.
- 548 Zachos, J. C., Pagani, M., Sloan, L., Thomas, E. and Billups, K.: Trends, rhythms,  
549 and aberrations in global climate 65 Ma to present., *Science*, 292(5517), 686–693,  
550 2001a.
- 551 Zachos, J. C., Shackleton, N. J., Revenaugh, J. S., Pälike, H., and Flower, B. P.,  
552 Periodic and non-periodic climate response to orbital forcing across the Oligocene-  
553 Miocene boundary. *Science*. 292, 274-277, 2001b
- 554 Zachos, J. C., Kroon, D. and Blum, P.: ODP Leg 208: The early Cenozoic extreme  
555 climates transect along walvis ridge, *Proceedings of the Ocean Drilling Program*  
556 *Initial Reports*, 208, 2004.
- 557 Zachos, J.C., Röhl, U., Schellenberg, S.A., Sluijs, A., Hodell, D.A., Kelly, D.C.,  
558 Thomas, E., Nicolo, M., Raffi, I., Lourens, L.J., McCarren, H., and Kroon, D.: Rapid  
559 acidification of the ocean during the Paleocene-Eocene thermal maximum.: *Science*  
560 (New York, N.Y.), v. 308, no. 5728, p. 1611–5, doi: 10.1126/science.1109004, 2005.
- 561 Zachos, J. C., Dickens, G. R. and Zeebe, R. E.: An early Cenozoic perspective on  
562 greenhouse warming and carbon-cycle dynamics., *Nature*, 451(7176), 279–283,  
563 doi:10.1038/nature06588, 2008.
- 564 Zachos, J. C., McCarren, H., Murphy, B., Röhl, U. and Westerhold, T.: Tempo and  
565 scale of late Paleocene and early Eocene carbon isotope cycles: Implications for the  
566 origin of hyperthermals, *Earth Planet. Sci. Lett.*, 299(1-2), 242–249,  
567 doi:10.1016/j.epsl.2010.09.004, 2010.
- 568 Zeebe, R. E. and Zachos, J. C.: Long-term legacy of massive carbon input to the Earth  
569 system: Anthropocene versus Eocene., *Philos. Trans. A. Math. Phys. Eng. Sci.*,  
570 371(2001), 2013.
- 571

572 TABLE 1: Age-depth tie points based on the tuning of the filtered 3 m- period extracted from  
 573 Site 1262 color reflectance record and the long eccentricity cycle extracted from the Laskar  
 574 solution La2010d (Laskar et al., 2011).

575

<b>Site 1262 3-m period filter</b>	<b>Long eccentricity cycle (kyrs)</b>	
	<i>Laskar 2010d</i>	<i>Laskar 2010d</i>
	<b>(Option 1)</b>	<b>(Option 2)</b>
102.750	51800	52206
104.231	52003	52410
105.711	52206	52614
107.167	52410	52816
108.648	52614	53017
110.129	52816	53216
111.635	53017	53415
113.193	53216	53615
114.750	53415	53815
116.359	53615	54016
117.865	53815	54218

576

577 TABLE 2: Color reflectance tie points from ODP Site 1263 and Site 1262 and interpolated  
 578 ages obtained from the astronomically tuned age model.

Samples	Site 1263 Depth (mbsf)	Site 1263 Depth (mcd)	Samples	Site 1262 Depth (mbsf)	Site 1262 Depth (mcd)	Interpolated Age (Ma)	
						Option 1	Option 2
1263A-26H-4, 147.5	228.575	265.425	1262B-11H-4, 137.5	92.275	101.855	51.610	52.014
1263A-26H-5, 50	229.1	265.95	1262B-11H-5, 42.5	92.825	102.405	51.727	52.132
1263A-26H-5, 90	229.5	266.35	1262B-11H-5, 102.5	93.425	103.005	51.835	52.241
1263A-26H-5, 115	229.75	266.6	1262B-11H-5, 137.5	93.775	103.355	51.883	52.289
1263A-26H-6, 147.5	231.575	268.425	1262B-11H-6, 45	94.35	103.93	51.962	52.369
1263A-26H-7, 30	231.9	268.75	1262A-10H-2, 120	88.2	104.31	52.014	52.421
1263B-22H-5, 100	230.9	269.23	1262A-10H-2, 145	88.45	104.56	52.048	52.455
1263B-22H-5, 125	231.15	269.48	1262A-10H-3, 20	88.7	104.81	52.082	52.490
1263B-22H-6, 142.5	232.825	271.155	1262A-10H-3, 60	89.1	105.21	52.137	52.545
1263B-22H-7, 45	233.35	271.68	1262A-10H-3, 87.5	89.375	105.485	52.175	52.583
1263A-27H-1, 65	232.75	272.78	1262A-10H-4, 2.5	90.025	106.135	52.265	52.673
1263A-27H-2, 7.5	233.675	273.705	1262A-10H-4, 27.5	90.275	106.385	52.300	52.707
1263A-27H-2, 17.5	233.775	273.805	1262A-10H-4, 37.5	90.375	106.485	52.314	52.721
1263A-27H-2, 25	233.85	273.88	1262A-10H-4, 45	90.45	106.56	52.325	52.732
1263A-27H-2, 125	234.85	274.88	1262A-10H-4, 77.5	90.775	106.885	52.370	52.777
1263A-27H-2, 145	235.05	275.08	1262B-12H-1, 70	96.6	107.24	52.420	52.826
1263A-27H-3, 40	235.5	275.53	1262B-12H-1, 85	96.75	107.39	52.441	52.846
1263A-27H-3, 67.5	235.775	275.805	1262B-12H-1, 100	96.9	107.54	52.461	52.867
1263A-27H-3, 100	236.1	276.13	1262B-12H-1, 110	97	107.64	52.475	52.880
1263A-27H-3, 135	236.45	276.48	1262B-12H-1, 120	97.1	107.74	52.489	52.894
1263A-27H-4, 77.5	237.375	277.405	1262B-12H-2, 5	97.45	108.09	52.537	52.941
1263A-27H-4, 100	237.6	277.63	1262B-12H-2, 22.5	97.625	108.265	52.561	52.965
1263A-27H-4, 137.5	237.975	278.005	1262B-12H-2, 60	98	108.64	52.613	53.016
1263A-27H-5, 70	238.8	278.83	1262B-12H-2, 110	98.5	109.14	52.681	53.083
1263C-9H-4, 105	240.45	280.24	1262B-12H-2, 135	98.75	109.39	52.715	53.117
1263C-9H-5, 15	241.05	280.84	1262B-12H-3, 12.5	99.025	109.665	52.753	53.154
1263C-9H-5, 100	241.9	281.69	1262B-12H-3, 40	99.3	109.94	52.790	53.191
1263C-9H-6, 2.5	242.425	282.215	1262B-12H-3, 57.5	99.475	110.115	52.814	53.214
1263C-9H-6, 15	242.55	282.34	1262B-12H-3, 65	99.55	110.19	52.824	53.224
1263C-9H-6, 32.5	242.725	282.515	1262B-12H-3, 85	99.75	110.39	52.851	53.251
1263C-9H-6, 82.5	243.225	283.015	1262B-12H-4, 10	100.5	111.14	52.951	53.350
1263A-28H-1, 40	242	284.52	1262B-12H-4, 65	101.05	111.69	53.024	53.422
1263A-28H-1, 95	242.55	285.07	1262B-12H-4, 122.5	101.625	112.265	53.097	53.496
1263A-28H-1, 115	242.75	285.27	1262A-11H-1, 137.5	96.375	112.425	53.118	53.516
1263A-28H-2, 40	243.5	286.02	1262A-11H-2, 2.5	96.525	112.575	53.137	53.536
1263A-28H-2, 70	243.8	286.32	1262A-11H-2, 12.5	96.625	112.675	53.150	53.549
1263A-28H-2, 107.5	244.175	286.695	1262A-11H-2, 50	97	113.05	53.198	53.597
1263A-28H-3, 5	244.65	287.17	1262A-11H-2, 67.5	97.175	113.225	53.220	53.619
1263A-28H-3, 27.5	244.875	287.395	1262A-11H-2, 80	97.3	113.35	53.236	53.635
1263A-28H-3, 32.5	244.925	287.445	1262A-11H-2, 85	97.35	113.4	53.243	53.642

---

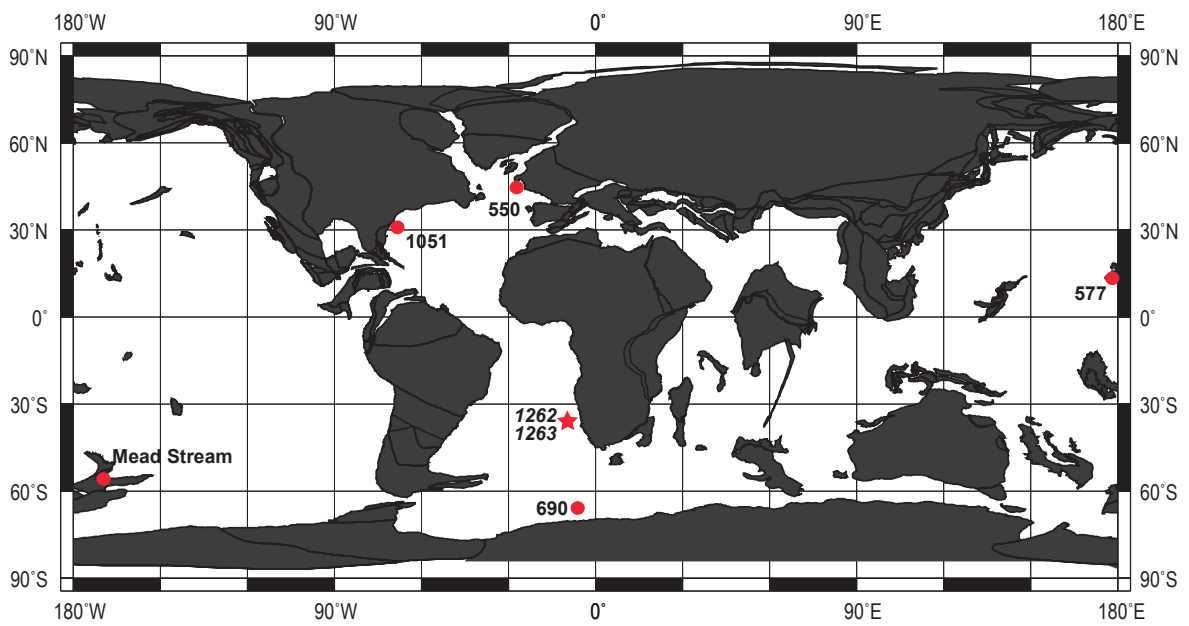
1263A-28H-3, 65	245.25	287.77	1262A-11H-2, 97.5	97.475	113.525	53.258	53.658
1263A-28H-3, 70	245.3	287.82	1262A-11H-2, 105	97.55	113.6	53.268	53.667
1263B-24H-2, 147.5	245.875	288.165	1262A-11H-2, 132.5	97.825	113.875	53.303	53.703
1263B-24H-3, 67.5	246.575	288.865	1262A-11H-2, 147.5	97.975	114.025	53.322	53.722
1263B-24H-4, 135	248.75	291.04	1262A-11H-3, 95	98.95	115	53.446	53.846
1263B-24H-5, 47.5	249.375	291.665	1262A-11H-3, 145	99.45	115.5	53.508	53.909
1263B-24H-6, 20	250.6	292.89	1262A-11H-4, 52.5	100.025	116.075	53.580	53.981
1263C-10H-5, 65	251.05	292.93	1262A-11H-4, 57.5	100.075	116.125	53.586	53.987
1263C-10H-5, 82.5	251.225	293.105	1262A-11H-4, 72.5	100.225	116.275	53.605	54.006
1263C-10H-5, 110	251.5	293.38	1262A-11H-4, 87.5	100.375	116.425	53.624	54.025
1263C-10H-7, 1	252.91	294.79	1262A-11H-4, 135	100.85	116.9	53.687	54.089
1263C-10H-7, 5	252.95	294.83	1262A-11H-5, 5	101.05	117.1	53.713	54.089
1263C-10H-7, 10	253	294.88	1262A-11H-5, 10	101.1	117.15	53.720	54.122

579

580 **FIGURES**

581 **Figure 1:** Paleogeographic reconstruction for the early Eocene (~54 Ma) showing the  
582 approximate position of Sites 1263 and 1262 (Walvis Ridge), (map provided by  
583 Ocean Drilling Stratigraphic Network, ODSN;  
584 <http://www.odsn.de/odsn/services/paleomap/paleomap.html>, modified). Also shown  
585 the locations of ODP Sites 690 and 1051 and DSDP Sites 550 and 577 (Cramer et al.  
586 2003) and Mead Stream (Slotnick et al. 2012).

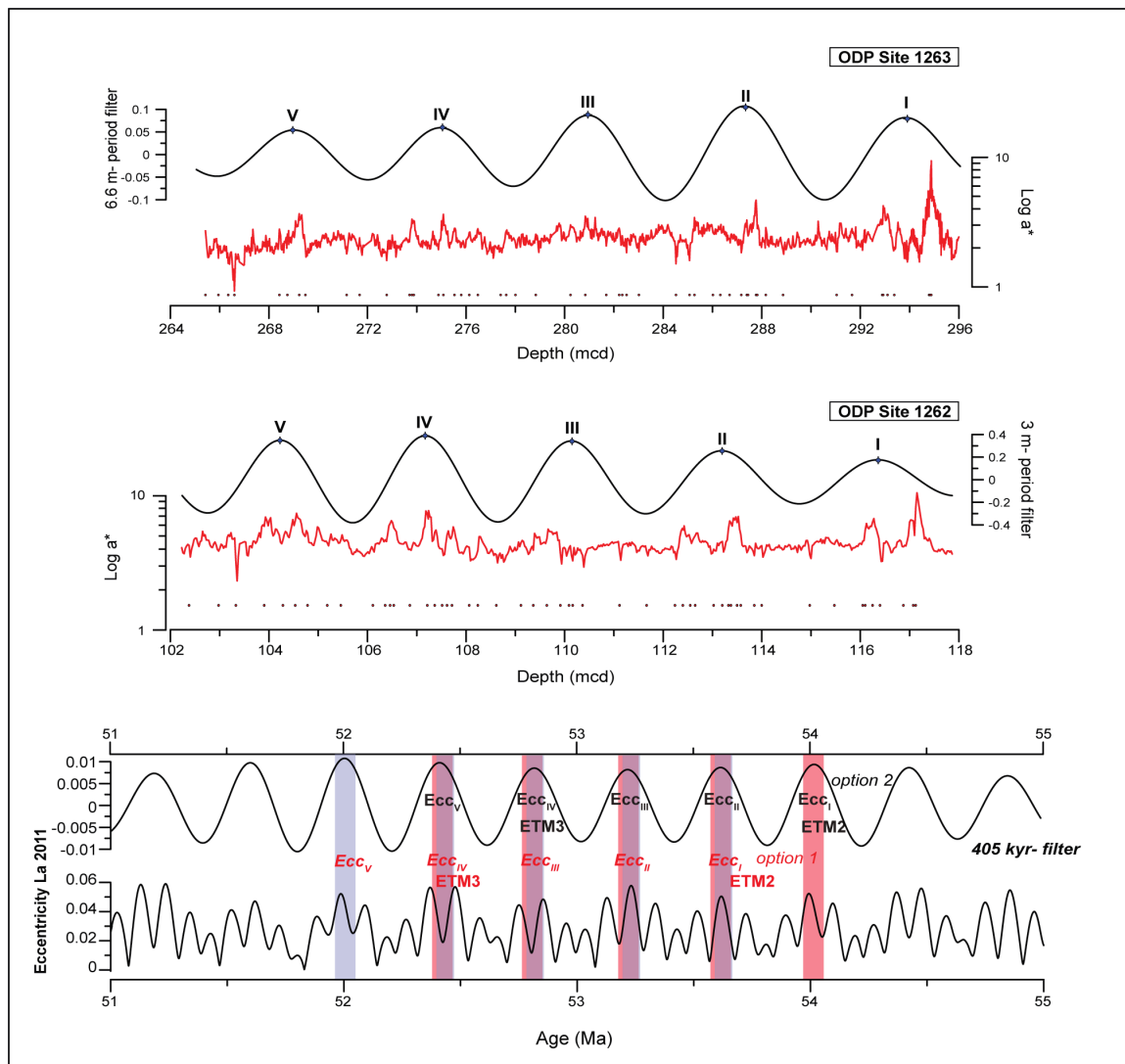
587



588

589

590 **Figure 2:** The floating orbitally tuned age model was constructed based on the red  
 591 over green color ratio ( $a^*$ ) records of ODP Sites 1263 and 1262. The extracted ~3-m  
 592 period from Site 1262 was used to tune the record to the extracted 405-kyr  
 593 eccentricity component of the La2010d orbital solution (Laskar et al., 2011), with  
 594 maximum  $a^*$  values corresponding to maximum eccentricity values. Interpolated ages  
 595 were transferred then to Site 1263 by using age-depth tie points (black dots).  
 596 Uncertainties in dating proxies prevent an absolute age for this time interval, anchored  
 597 to the lack of an absolute age for the PETM. Therefore, different tuning options are  
 598 available within an 800 kyr window (Westerhold et al., 2008). Two possible options  
 599 are shown.

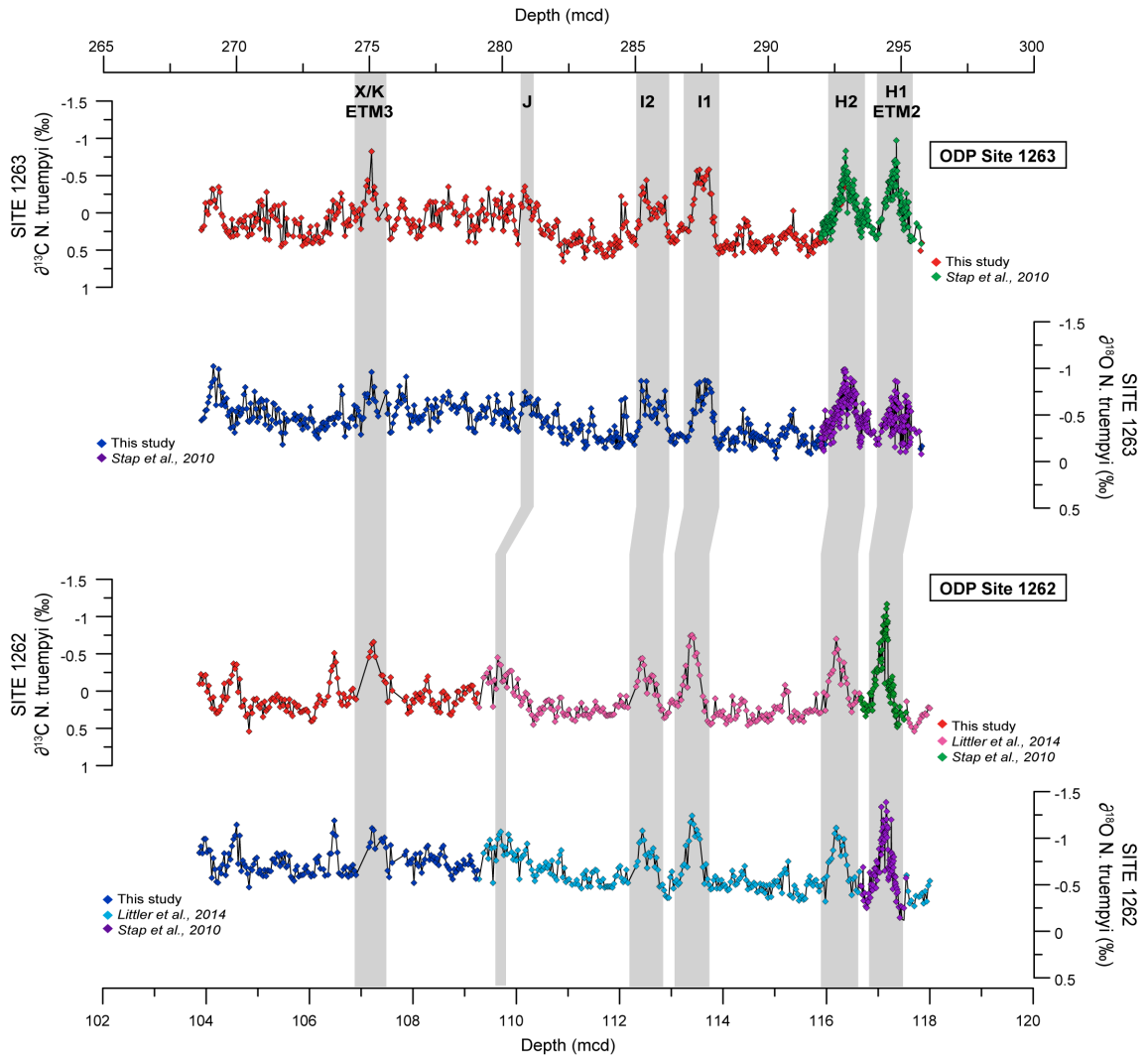


600

601

602

603 **Figure 3:** Benthic *N. truempyi*  $\delta^{13}\text{C}$  and  $\delta^{18}\text{O}$  records from Site 1263 and Site 1262,  
604 plotted versus depth. Highlighted intervals represent the position of the early Eocene  
605 hyperthermal events.

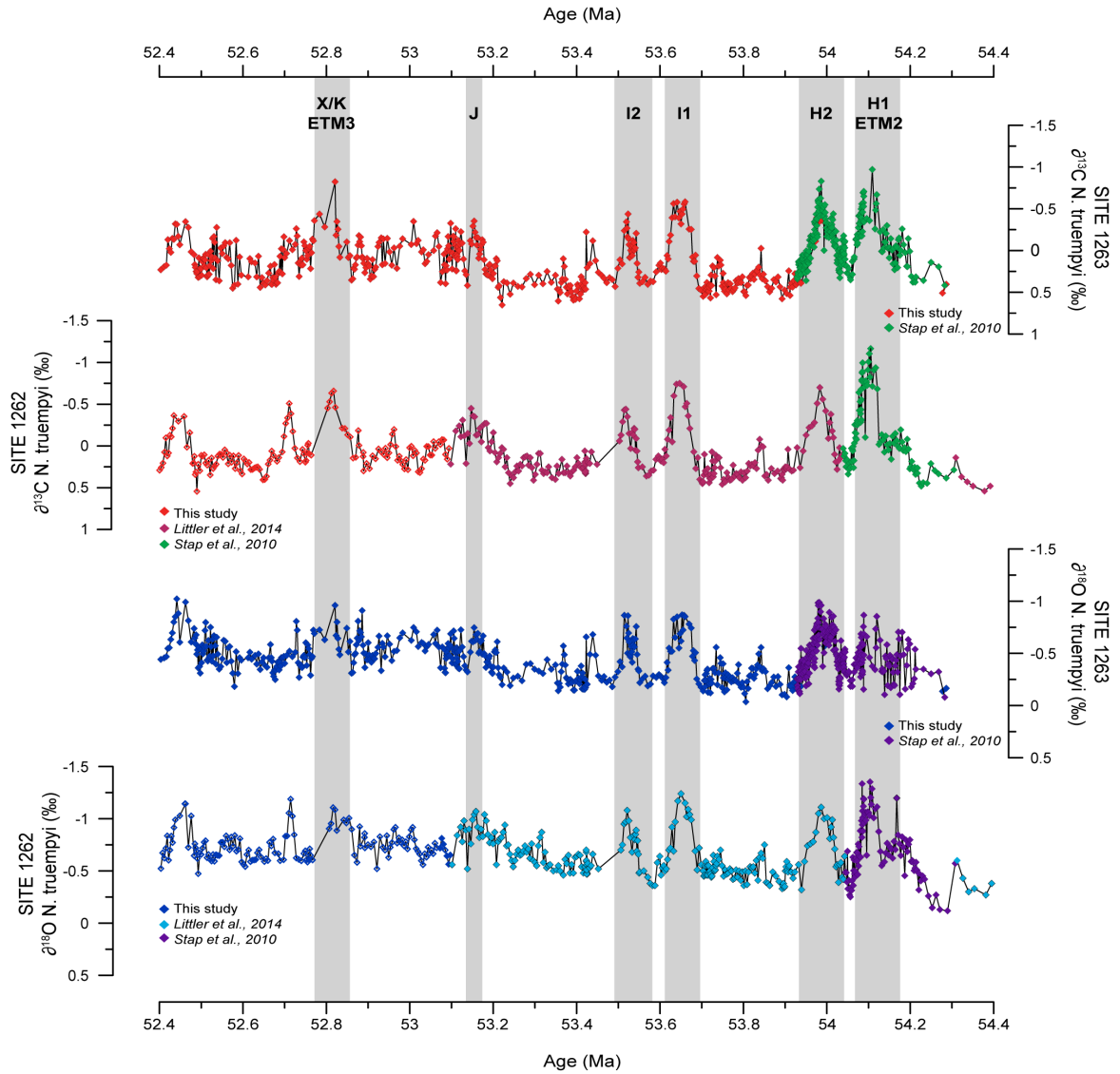


606

607



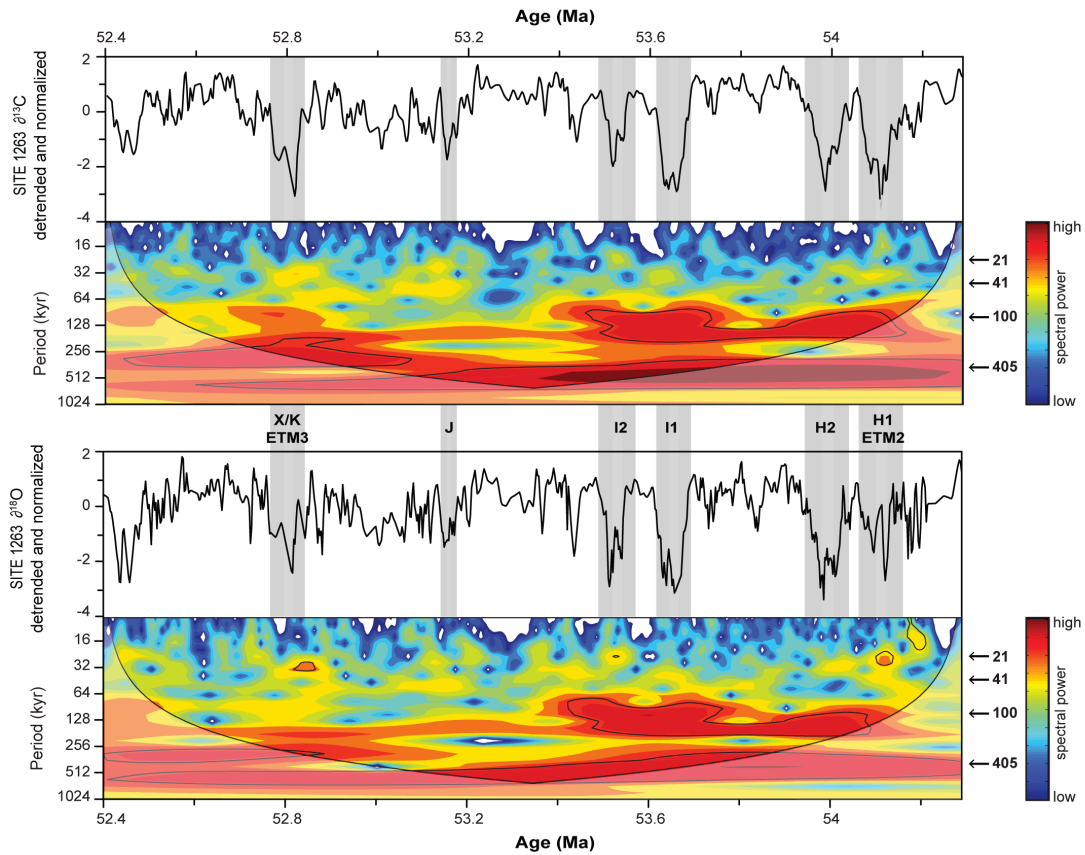
608 **Figure 4:** Benthic *N. truempyi*  $\delta^{13}\text{C}$  and  $\delta^{18}\text{O}$  records from Site 1263 and Site 1262,  
 609 plotted versus Age (Ma), (starting from option 2 for the age of ETM2- Westerhold et  
 610 al., 2008). Highlighted intervals represent the position of the early Eocene  
 611 hyperthermal events.



612

613

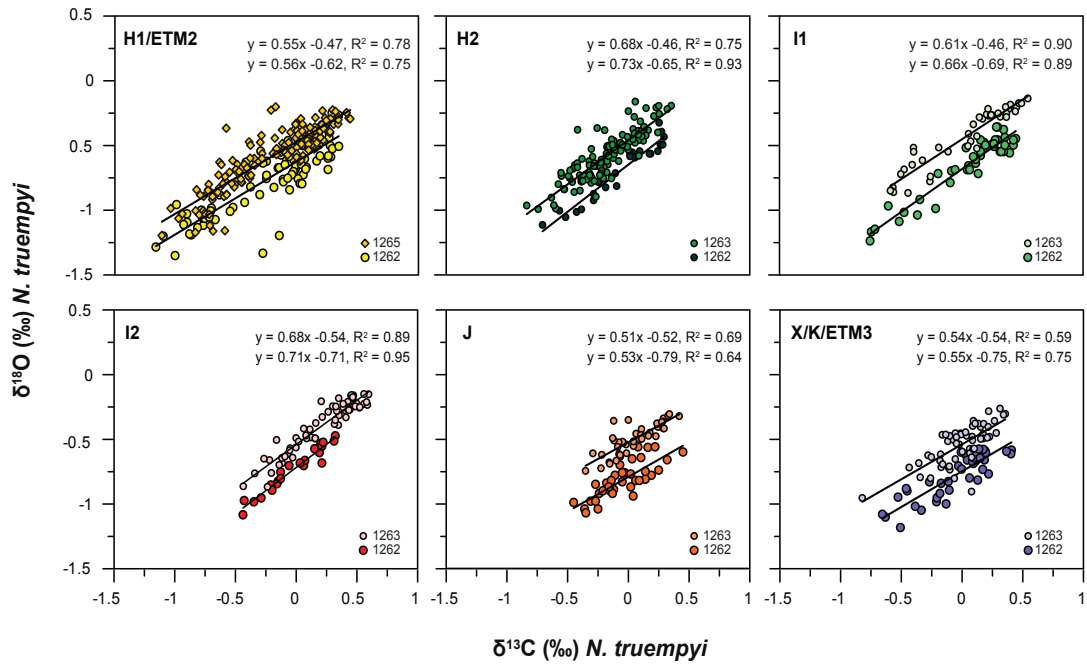
614 **Figure 5:** Evolutionary wavelet analyses for  $\delta^{13}\text{C}$  and  $\delta^{18}\text{O}$  were performed using a  
615 Morlet mother wavelet of an order of 6. The shaded area represents the 95%  
616 significance level. Spectral power above the confidence level is concentrated at  
617 distinct frequencies, corresponding to the long 405-kyr and short eccentricity 100-kyr  
618 cycles. Highlighted intervals represent the position of the early Eocene hyperthermal  
619 events.



620

621

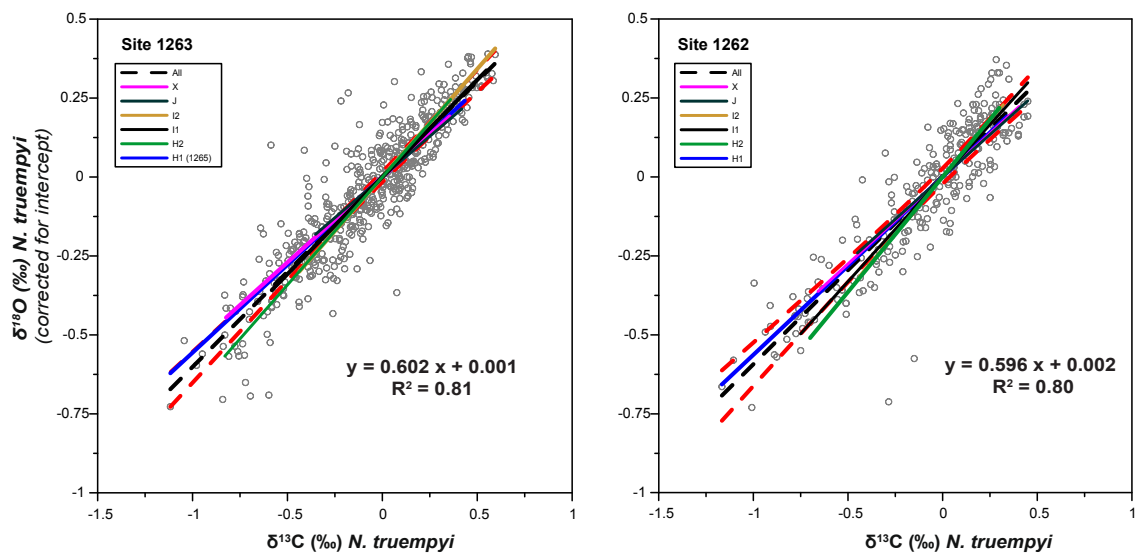
622 **Figure 6:** Relationship between the oxygen and carbon isotope values of *N. truempyi*  
 623 during ETM2, H2, I1, I2, J and ETM3/X at Site 1263 and Site 1262. Data for ETM2  
 624 and H2 from Stap et al. (2010) and for I1, I2 and J at Site 1262 from Littler et al.  
 625 (2014). Note that, because of intense dissolution at Site 1263, ETM2 data were  
 626 chosen from Site 1265. For all the events, throughout the entire event (onset+recovery  
 627 phases), changes in the exogenic carbon pool are linearly related to warming. Linear  
 628 regression equations refer to Site 1263 (top) and Site 1262 (bottom), respectively.



629

630

631 **Figure 7:** Slope of each event plotted together with the average slope (from all the  
632 events). The red dashed line indicates the 99% confidence interval.



633